1   **The marine methane cycle in the Canadian Arctic Archipelago during summer.**

2   Alessandra D'Angelo[1], Cynthia Garcia-Eidell[2], Zak Kerringan[1], Jacob Strock[1], Frances Crable[2], Nikolas
3   VanKeersbilck[3], Humair Raziuddin[2], Theressa Ewa[2], Samira Umar[2], Andrew L. King[4], Miquel Gonzelez-
4   Meler[2] and Brice Loose[1]
5
6   [1]University of Rhode Island, Graduate School of Oceanography, Narragansett, RI 02882, USA
7   [2]University of Illinois at Chicago, Chicago, IL 60607, USA
8   [3]University of Iceland, 102 Reykjavík, Iceland
9   [4]Norwegian Institute for Water Research, 0579 Oslo, Norway
10
11   Corresponding author: Alessandra D'Angelo, a_dangelo@uri.edu
12

13   **Abstract**

14   In the Arctic Ocean region, methane (CH_4) concentrations are higher than the global average, with
15   particularly high concentrations of dissolved CH_4 observed along many subarctic and Arctic continental
16   shelf margins. Despite this, the Arctic Ocean emits only minimal methane fluxes to the atmosphere across
17   the air-sea interface, suggesting that water column oxidation of methane may be an important process.
18   In this study, we paired thermohaline, chemical, and biological data collected during the Northwest
19   Passage Project transit through the Canadian Arctic Archipelago (CAA) waters in the summer of 2019 with
20   in-situ and in-vitro methane data. Our findings suggested that the most elevated in-situ concentration of
21   dissolved methane was present in the near-surface waters of the Pacific, particularly in meltwater regions.
22   The highest methane concentrations were observed within shallow waters, averaging at 5.8±2.5 nM within
23   the upper 30m depth. Furthermore, the methane distribution showed a distinct pattern from east to west,
24   with higher concentrations and oxidation rate potential in the western region. In our study, we observed
25   generally low methane oxidation rate constants, averaging at 0.006±0.002 d^{-1}. However, surface waters
26   from Wellington Channel and Croker Bay exhibited relatively higher methane oxidation rates, averaging at
27   0.01±0.0004 d^{-1}. These regions were distinguished by a significant proportion of meltwater, including both
28   meteoric water and sea ice meltwater, mixed with water of Pacific origin. We identified microbial taxa of
29   Pacific-origin likely associated with methane oxidation, including *Oleispira* (γ-proteobacteria) and
30   *Aurantivirga* (Flavobacteria), in the Pacific and meteoric waters. In contrast, deeper layers (>200m depth)
31   showed lower methane concentrations (av. 3.1±1.1 nM) and lower methane oxidation rate constants (av.
32   0.005±0.001 d^{-1}). Within the sea ice, dissolved methane concentrations were found to be higher than the
33   concentrations at equilibrium with atmospheric capacity, with an average of [CH_4]=9.2±5 nM. The sea ice
34   temperature data (Table S2) indicated the presence of ice permeability, which likely facilitated the release
35   of dissolved methane that was either trapped or produced since the previous freezing period. Notably,
36   methane concentrations were 25% higher in waters collected in the western CAA in comparison to the ice-
37   free waters (eq. S1).
38   The overall picture suggested supersaturation of in-situ methane in shallow waters, coupled with
39   faster oxidation rates in meltwater and Pacific dominant layers, suggesting rapid seasonal cycling of
40   methane and prevention of the methane migration into the atmosphere.
41

42   **1. Introduction**

43   Methane (CH_4) is a significant climate-relevant gas with a global warming potential 28 times
44   greater than carbon dioxide (CO_2) over a 100-year timescale (Pachauri et al., 2014). It is the second most

45 significant greenhouse gas after carbon dioxide, contributing to approximately 23% of climate change in
46 the twentieth century. Anthropogenic emissions from agricultural practices, fossil fuel production, and
47 waste disposal account for most of the methane released into the atmosphere, while minor sources such as
48 wildfire, biomass burning, permafrost, termites, dams, and the ocean, contribute to the remaining 20%
49 (Saunois et al., 2020). Methane concentrations in the Arctic region are 8-10% higher than the global
50 average, with a dry air mole fraction of 1890 ppb (Saunois et al., 2020; Oh et al., 2020). Recent studies
51 have measured elevated concentrations of dissolved CH_4 in the subarctic and Arctic shelf areas, with limited
52 gas exchange at the air-sea interface (e.g., Fisher et al., 2011; Shakhova et al., 2014; Steinle et al., 2015;
53 Ferré et al., 2020).
54 In-situ measurements of methane concentration in the water column can reveal information about past
55 processes that have affected its distribution. Methane is relatively stable in the water column, persisting for
56 a significant amount of time after it has been produced, transported, or dissolved (Yamamoto et al., 1976).
57 Therefore, in-situ measurements can provide a historical record of methane in the water column. In contrast,
58 in-vitro methane experiments, such as methane oxidation rate assays, provide information on the potential
59 microbial processes that could occur. These experiments measure the rate at which methane is consumed
60 by microorganisms present in the water sample. This information helps to understand the potential for
61 methane to be removed from the water column through microbial processes and provides insight into the
62 cycling of methane. Hence, understanding the role of marine microbial metabolism in methane production
63 and oxidation is crucial for assessing the amount of methane vented into the atmosphere. Environmental
64 drivers control the methanotrophy (microbial aerobic oxidation of methane) by supplying suitable
65 substrates for metabolic processes (Singh et al., 2010). Observations of microbial community structure can
66 be used to identify ecosystem states, estimate biological activity rates, and better understand the
67 mechanisms underlying changes in biogeochemical processes. Previous studies have investigated the
68 methane flux in various regions of the Arctic Ocean, including the Northwest Passage (NWP), and assessed
69 the methane budget (Kitidis et al., 2010; Damm et al., 2010; Sultan et al., 2020; Manning et al., 2020, 2022).
70 In the NWP, methane undersaturation was attributed to meltwater, while methane oversaturation was
71 detected underneath multi-year sea ice (Kitidis et al., 2010). Multi-year observations have suggested that
72 riverine freshwater is not a major source of CH_4 in the Canadian Arctic Archipelago (CAA), at least during
73 summer and early fall (Manning et al., 2022). Furthermore, it was determined that the rate of CH_4 exchange
74 between the ocean and atmosphere was low, indicating that this region has a minor role in regulating global
75 atmospheric concentrations of methane across the North American Arctic Ocean (Manning et al., 2020,
76 2022). Therefore, the primary sources of CH_4 in the CAA remain poorly identified.
77 This study aims to further elucidate the methane cycle in the NWP, quantify seawater methane
78 oxidation as a sink, and detect its main association with environmental features and biogenic control in the
79 water column. These analyses are supported by thermohaline, chemical, and biological characteristics of
80 the water masses in relation to the methane cycle. The uniqueness of this study lies in the analysis of paired
81 datasets of dissolved methane and potential oxidation rates with associated marine microbial communities
82 and physical-chemical properties of the water masses in the CAA, such as temperature, salinity,
83 chlorophyll-α fluorescence, turbidity, and nutrients.
84
85 **1.2 Study area**
86 The study area was centered around Parry Channel, between 71 – 77 ºN, and 100 – 79 ºW (Fig. 1).
87 From East to West, named parts of the Channel are, Lancaster Sound, Barrow Strait, and Melville Sound.
88 This Channel connects Baffin Bay to the east with the Beaufort Sea to the west.
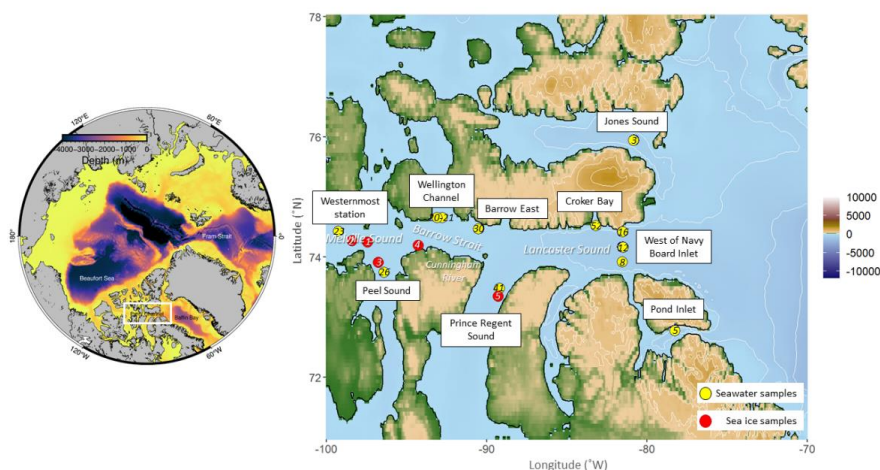
Figure 1: The left panel displays the bathymetric chart of the Arctic Ocean, with the study area delineated by a white rectangle. The right panel shows the study area during the Northwest Passage cruise in July-August 2019, with sampling stations represented by yellow dots and sea ice coring sites by red dots.

The Arctic Ocean (AO) features a vast estuarine system that exerts thermohaline (buoyancy) forcing on the inputs and disposition of freshwater components (Stigebrandt, 1984; Carmack et al., 2016). The Canadian Arctic Archipelago (CAA) serves as a watershed discharge in the AO, as it receives advection from the relatively fresh upper layers of the AO, ice melt, local river discharge, and net precipitation (Ingram and Larouche, 1987). One of three main routes connecting the AO to the Labrador Sea and the North Atlantic is the Northwest Passage (McLaughlin et al., 2007). A limiting sill is present in the Lancaster Sound further east in Barrow Strait, where the depth is approximately 125 m. Continuing eastward, water depths increase gradually to approximately 500m in Lancaster Sound, then sharply to over 2000 m in the center of Baffin Bay (McLaughlin et al., 2007). The flow through the CAA, from the Pacific to the Arctic to the Atlantic Oceans, results from the higher sea level of the Pacific Ocean (McLaughlin et al., 2007). This sea level difference arises because Pacific waters (PW) are fresher, and assuming a level of no-motion among the three ocean basins, the Arctic is thought to be 0.15 m higher than the Atlantic (Stigebrandt, 1984). During the eastward transit through Parry Channel, the PW and Atlantic Water (AW) undergo mixing. The shallow sill at Barrow Strait restricts the eastward flow across Lancaster Sound, constraining the deep layer of AW (McLaughlin et al., 2007). The riverine runoff supplied by Cunningham River, Garnier River, and Mecham River has a significant impact on the hydrodynamics and biogeochemistry of Lancaster Sound (Brown et al., 2020). The Special Report on the Ocean and Cryosphere in a Changing Climate published by the IPCC in 2021 showed that the runoff into the AO increased by $3.3 \pm 1.6\%$ and $2.0 \pm 1.8\%$ for Eurasian and North American rivers, respectively (1976–2017). Tidal energy also affects the hydrodynamics within Parry Channel, entering the CAA primarily from the Atlantic Ocean and being mainly semi-diurnal. As a result, waters transiting the Northwest Passage are significantly modified by tidally-driven mixing, and tidal currents are particularly strong, reaching 50–150 cm s^{-1} in the vicinity of Barrow Strait (Prinsenberg and Bennetr, 1989).

118   The water column structure is characterized by AW in the deep layers, with Pacific-origin waters
119   overlaid, and seasonal mixed water at the top (McLaughlin et al., 2007). In the summer, the seasonal mixed
120   layer (Polar Mixed Layer, PML) contains freshwater from river outflow and sea-ice melt, characterized by
121   low salinities, warm temperatures, low nutrient concentrations, and high dissolved oxygen saturations. This
122   water constitutes the uppermost layer, and its depth varies according to the meltwater supply (approximately
123   50 m deep in Parry Channel). Below this layer is the Pacific-origin summer water, which is characterized
124   by relatively warm temperatures and higher salinities, with higher nutrient concentrations and decreasing
125   oxygen saturations. Atlantic-origin water in deep layers shows maximum nutrient concentrations
126   (McLaughlin et al., 2007). The western part of the CAA is characterized by more consistent sea-ice
127   coverage compared to the eastern side (Agnew and Howell, 2003). According to data released by the
128   Canadian Ice Service, the thickness of first-year sea ice in the CAA can vary between 2.5 m and 2.0 m in
129   the northern and southern sections, respectively, with multi-year ice reaching a thickness of 3–5 m
130   (Canadian Ice Service, 2002). From the time of freeze-up in January to the break-up in late July, the ice is
131   usually immobilized as landfast ice, and is frequently accompanied by polynyas because of strong winds
132   (Dunbar, 1969).
133
134   **2. Materials and methods**
135   The list of the sampling locations and their acronyms used in this paper is the following (Fig. 1):
136   Westernmost station (WS), Wellington Channel (WC), Peel Sound (PS), Prince Regent Sound (PRS), West
137   of Navy Board Inlet (WNBI), Crocker Bay (CB), Jones Sound (JS), Pond Inlet (PI).
138
139   **2.1 Sampling procedures**
140   Seawater and sea ice samples were collected in the vicinity of Parry Channel during the Northwest
141   Passage Project cruise held between 17 July – 4 August 2019 onboard the Swedish icebreaker RVIB Oden.
142   The stations include both single points and transects (see Fig. 1), covering the area with longitude 78°14.94'
143   W - 99°16.63' W. Seawater was collected using a SeaBird 32 Water Carousel CTD rosette (24 x 12L), set
144   with a SeaBird SBE 911+ CTD with dissolved oxygen and WETLabs Ecopuck sensors. The CTD sensor
145   was owned and calibrated by the Swedish Polar Research Secretariat (SPRS). CTD casts and rosette bottle
146   data are hosted at Swedish National Data Service (https://snd.gu.se/en/catalogue/study/2021-119#dataset),
147   whereas   the   whole   dataset   and   the   processed   CTD   data   are   stored   in   Arcticdata.io
148   (https://doi.org/10.18739/A2BN9X45M).
149   The sea ice concentration data was provided by the University of Bremen data archive, with 1-km space
150   resolution (seaice.uni-bremen.de, Ludwig et al., 2019 and 2020). Sea ice charts from the Canada Ice Center
151   were   also   used   (www.canada.ca/en/environment-climate-change/services/ice-forecasts-
152   observations/publications/interpreting-charts).
153   *Methane* – A total of 132 seawater samples (28x2 experimental and 76 discrete) (Table S1), and 5
154   sea ice cores (Table S2), were collected and analyzed to determine methane concentration and isotopic
155   ratio. The sea ice cores were sampled using a Kovacs ice corer drill, while seawater was sampled through
156   the CTD rosette as previously described. Sea ice was examined for in-situ dissolved methane, while in
157   seawater, we also measured the microbial oxidation rates. Methane concentrations and isotopic ratios were
158   analyzed in both in-situ and in-vitro samples using the method described by Uhlig and Loose (2017).
159   Together, in-situ measurements and in-vitro experiments provide complementary information on methane
160   in the water column. In-situ measurements reveal the past processes that have influenced methane
161   concentrations, while in-vitro experiments provide insight into the potential for methane metabolism and

162   removal from the water column. All the samples were collected using multi-layer foil gas sampling bags
163   (Restek, Bellfonte, PA – USA) and processed for further analysis following the details provided in
164   paragraphs 2.2 and 2.3.

165   *Microbial community* – A total of 18 seawater samples were obtained from the in-vitro methane
166   incubations at the end of the experiments to identify the most abundant microbial taxa. These samples were
167   then juxtaposed with in-situ samples for comparative analysis. To collect the samples, a cylindrical, 0.22
168   µm Sterivex membrane filter (Millipore Sigma, Billerica, MA) was attached to the valve of each bag. DNA
169   was extracted from the filters by drawing water from the Sterivex filter. The filters were then stored at -80
170   °C until they were transported to the University of Rhode Island (URI), Graduate School of Oceanography
171   (GSO) for DNA extraction using the DNeasy PowerWater Sterivex Kit (Qiagen, Germantown, MD),
172   following the manufacturer's protocol (See paragraph 2.4 for further details).

173   *Nutrients* – A total of 239 seawater samples were collected to measure nutrients (doi:
174   10.18739/A2BN9X45M). Each sample had a volume of approximately 45 mL and was filtered through a
175   0.22-micron Millex-GP Sterile Syringe Filter with PES Membrane (Thermo Fisher Scientific). The filtered
176   samples were transferred to a Corning Falcon 50 mL Conical Centrifuge Tube (Fisher Scientific) and stored
177   at -20°C onboard RVIB Oden for post-cruise analysis. Although the nutrient results are not discussed in
178   this context, they will be utilized in the analysis to determine the Arctic Nitrate-Phosphate tracer in the
179   water mass analysis, as described in Jones et al. (1998) and Tomczak (1981).

180          $\delta^{18}O$-Salinity - A total of 125 water samples were collected from 52 CTD casts following the
181   CLIVAR/GO-SHIP protocol to investigate $\delta^{18}O$-Salinity relationship. To collect samples for water stable
182   isotopes analyses, 30-mL Nalgene bottles were filled to the brim, tightly closed, sealed with parafilm, and
183   stored in labeled sample bags. Two samples were taken per depth. All water samples were transported to
184   the Atmosphere, Climate, and Ecosystems lab at University of Illinois at Chicago (UIC) for processing.
185   The $\delta^{18}O$-Salinity dataset, which comprises more than 200 new and paired $\delta^{18}O$-Salinity measurements in
186   the CAA, is publicly available through Pangaea at https://doi.pangaea.de/10.1594/PANGAEA.937543. As
187   for the nutrients data, we utilized the $\delta^{18}O$ samples to evaluate water mass fractions solving a simple 4-
188   endmember mass balance analysis, as described in Tomczak (1981) and developed by Östlund and Hut
189   (1984). For more information, refer to paragraph 2.5.

190

191   **2.2 Methane concentration and isotope ratio measurements for in-situ samples**
192   *Samples processing* –Seawater and sea ice for methane concentration and isotopic analysis was
193   collected through vacuum multi-layer foil gas sampling bags equipped with a polypropylene combo valve
194   and septum (capacity 3L, # 22951, Restek, Bellfonte, Pennsylvania, U.S.A.). For seawater, experiments
195   were performed with approximately 2.8 L. The sea ice cores were put in 3L bags and melted at room
196   temperature for the analysis. In all the bags a headspace of approximately 50 mL was created using
197   hydrocarbon-free air, and the samples were stored in water at room temperature (approximately 10°C).
198   Bags were analyzed for [CH$_4$] and isotopic signature ($\delta^{13}CH_4$) directly after preparation, following the
199   method of Uhlig and Loose (2017). For assessing the methane saturation of the seawater and sea ice, we
200   calculated the methane seawater and sea ice at equilibrium with the normal atmosphere, derived by the
201   Bunsen solubility coefficients (Gas-Solubility Codes in R, https://github.com/URIGSO/Gas-
202   Solubility-Codes), using in-situ potential temperature and practical salinity. The saturation anomaly was
203   calculated as ([CH$_4$]$_{in-situ}$ / [CH$_4$]$_{equilibrium}$ − 1) *100, considering the solubility of the atmospheric methane
204   at in-situ marine potential temperature and practical salinity.

205   *Calibration* - Standard gases 1001 (2500ppmv, $\delta^{13}CH_4$= -23.9 ‰), 1002 (250ppmv, $\delta^{13}CH_4$= -38.3
206   ‰), 1003 (2500ppmv, $\delta^{13}CH_4$= -66.5 ‰) (Isometrics, Victoria, British Columbia, Canada) were used to
207   generate linear calibrations for mixing ratios and isotope ratios in order to correct for any transient
208   deviations in the G2201-i analyzer, while the standard 1003 was used almost simultaneously during the
209   measurements to calibrate the measurements via daily drift (Uhlig and Loose, 2017). The 1003 standard
210   revealed distinct instrumental drift while onboard the vessel Oden, as compared to the measurements on
211   land; hence, we evaluated the dataset in two periods, from July 19th to August 4th (when the data were
212   measured at sea), and from August 5th to August 14th (when the data were measured in the National Science
213   Foundation facilities at Thule airbase, Greenland). The measurements of methane concentration were not
214   calibrated, because the standard deviation between replicate dissolved methane water samples was
215   significantly smaller than the standard deviation in gas standards that were introduced to the Picarro
216   analyzer, likely due to a manual artefact during syringe sampling of the gas standards. A complete
217   calibration of $\delta^{13}CH_4$ isotopic ratio was carried, because the isotope ratio was not affected in the same way
218   as concentration during syringe sample injection. For the isotope ratio, we calculated the slope and intercept
219   of the standard 1003 overtime and used the slope and intercept from the days of full calibrations (July 19
220   and July 29) into the equation for the data correction.

221    $$data.corrected = slope.day.cal * (data - std.1003.overtime) + (-66.5)$$

222   Where, -66.5 ‰ was the expected isotopic signature of the standard 1003.

223   *Quality control* – We ran multiple measurements for each sample, in order to assess the uncertainty
224   between the replicates and we only used data showing a standard deviation < 5% within the duplicated
225   measurements.
226

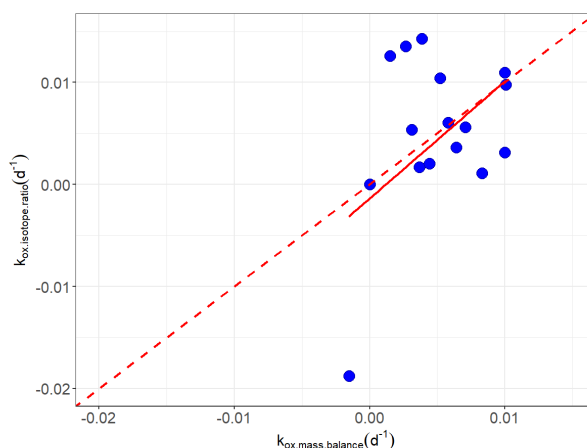**2.3 Methane concentration and isotope ratio measurements for in-vitro experiments**

228   We followed the methods of Uhlig and Loose (2017) with modifications.

229   *Samples processing* –Seawater for gas and isotope analysis was collected using vacuum multi-layer
230   foil gas sampling bags fitted with a polypropylene combo valve and septum (#22950 Restek, Bellfonte,
231   Pennsylvania, U.S.A.) with a capacity of 1 L. We used approximately 0.8-0.9 L seawater for each
232   experiment. The headspace was created with approximately 100 mL of hydrocarbon-free air, after which a
233   known volume (1 to 2.5 mL, as shown in Table S4) of gas standard 1003 with a known concentration and
234   isotopic composition (as described earlier) was injected into the samples. The samples were left for several
235   days before beginning the measurements. The incubation time ranged from 5 to 24 days (as indicated in
236   Table S3), which was driven by logistical constraints. As the stable isotope and mass balance method is
237   less sensitive to changes in methane, a longer incubation time was required compared to the radioisotope
238   method. Samples collected earlier in the cruise had a longer incubation time, while those collected towards
239   the end had a shorter time. Post-cruise, we extended the incubation times by continuing the analysis at a
240   laboratory in Thule Air Base. However, the extension period could not exceed 10 days. While the smallest
241   oxidation rates were not resolvable given the incubation time, we determined the lower limit using the
242   uncertainty, as reported in Uhlig and Loose (2017). The samples were stored in a cold room at
243   approximately 1°C throughout the experiment. For data calibration, we followed the same procedure used
244   for the in-situ samples.

245   *Estimating the oxidation rates from mass balance and isotopic fractionation* – Microbial methane
246   oxidation was quantified through incubation experiments using the method described in Uhlig and Loose
247   (2017). In each incubation, a known volume of methane standard 1003 was added to monitor changes in
248   mole and isotope ratio. In contrast to Uhlig and Loose (2017), we used an upper bound fractionation factor

249   α_{ox} of 1.025 to calculate the oxidation rate constant for isotopic ratio, as it was consistent with the values
250   obtained from the oxidation rate constants of the mass balance and isotope ratio (Fig. 2). The microbial
251   oxidation rates were determined from the first-order rate constant k_{ox} and the concentration of dissolved
252   methane in the water $[CH_4]_w$ during the incubation experiments, following the equation $r_{ox} = k_{ox} * [CH_4]_w$
253   (Uhlig and Loose, 2017). Figure 2 shows the trend line, which exhibited a Spearman's correlation of 0.52.
254

255
256   Figure 2: Comparison between first order oxidation rate constants (k_{ox}) determined from CH_4 concentration
257   (mass balance) and isotope ratios. The red line displayed the linear model between the values (R^2: 0.2564
258   p-value: 7.985e-12), whereas the red dashed line represented the 1:1 regression line.
259
260   Finally, to obtain an average k_{ox} value, we calculated the mean between $k_{ox.mass.balance}$ and $k_{ox.isotope.ratio}$. To
261   assess the success of the experiments and measure the microbial activity, a killed control was prepared for
262   each sample by adding 0.1M NaOH and injecting it into the sample after the final measurement. The $[CH_4]$
263   and $\delta^{13}C$-CH_4 were measured three times within a one-week time frame.
264   *Quality control* – We applied a stepwise criterion to evaluate and eliminate incubations of uncertain
265   outcome. Duplicate incubation samples were collected for every in-vitro determination of methane
266   oxidation rate. This resulted in a 2 by 2 matrix, with two independent measurements (mass balance and
267   isotopic fractionation) for each in-vitro bag, to ensure a robust determination of methane oxidation. The
268   following criteria were used to select the data for analysis:
269   1)   A significance test using the Student's T distribution was performed to ensure that the slope or rate
270   of change in $[CH_4]$ or $\delta^{13}CH_4$ vs. time (oxidation rate) was unique from zero, within error. A
271   confidence interval of 0.95 was chosen, and the number of independent measurements for each
272   incubation was less than 15 (N<15).
273   2)   The sign of k_{ox} from determinations from isotope ratio and molar mass determination for each
274   incubation bag were compared. The bags showing agreement between the isotope ratio and the
275   molar mass oxidation constants ($k_{ox.mass.balance}$ and $k_{ox.isotope.ratio}$ showing the same sign) were selected
276   for further analysis.
277   3)   In some cases, incubation bags agreed on the sign of k_{ox}, but either mass balance or isotope ratio
278   failed the significance test. For example, if $k_{ox.mass.balance}$ accepted the null hypothesis and $k_{ox.isotope.ratio}$

279   rejected it for the same sample, this estimate was flagged. If the replicate incubation bag agreed in
280   sign of k_{ox} with mass balance and isotope ratio passed the significance test, then the k_{ox} estimates
281   were included. This amounts to requiring at least 3 agreements within the 2 x 2 matrix criteria (2
282   for mass balance and 1 for isotope ratio, or vice versa) were selected. Overall, 37 incubation
283   estimates from $N_{tot}=56$ was eliminated by this criterion.

284   4) Finally, if replicated bags did not pass the significance test, these were counted as zero detectable
285   methane oxidation, suggesting this water sample did not come from water hosting active methane
286   oxidizing microbes. These were counted as zeros, rather than being eliminated (N = 2).

287   The analyses were performed using R version 4.1.2 in RStudio Version 1.2.5033. Plots were prepared using
288   the base and ggplot2 packages.

289

290   **2.4 DNA extraction and sequencing**

291   In this study, we analyzed the diversity of methane-oxidizing communities in seawater using 16S
292   rRNA gene sequencing. The analysis was performed on both in-situ water samples and methane-incubated
293   samples collected at the final time point of the experiment. The methods used for this analysis were in
294   accordance with the protocols described in Uhlig et al. (2018) and Kerrigan and D'Hondt (2022).

295   *DNA extraction* – DNA extraction was performed using the PowerWater® DNA extraction kit
296   (Qiagen, Germantown, MD) and the DNeasy PowerWater Sterivex Kit (Millipore® cat. no. SVGPL10RC).
297   The latter involved a novel filter membrane treatment, where lysis buffer was added to Sterivex units and
298   mixed, followed by additional mechanical lysis in a 5 ml bead beating tube. After protein and inhibitor
299   removal, genomic DNA was captured on an MB Spin Column under vacuum, washed, and eluted from the
300   MB Spin Column filter membrane in a 50–100 µl volume. The extracted DNA was of high quality and
301   suitable for downstream applications, including PCR and qPCR.

302   *PCR amplicon construction and sequencing* - To construct PCR amplicons, the V4-V5
303   hypervariable region of the 16S rRNA gene was amplified using forward and reverse primers from Parada
304   et al., 2016. The procedure described in Kerrigan and D'Hondt (2022) was followed. A 20-µl PCR reaction
305   was performed for each sample using 0.4 µl Platinum SuperFi II DNA Polymerase (Invitrogen, Carlsbad,
306   CA), 4 µl SuperFi II Buffer (5x), 0.2 mM dNTPs, 0.5 µM of each primer, and 0.1 µl Bovine Serum Albumin
307   (Thermo Scientific, Carlsbad, CA). Each water sample was amplified in a single PCR reaction with 5 µl of
308   DNA template. To account for possible PCR reagent contamination, three samples were amplified, each
309   one containing only laboratory water and no extract. Additionally, a sterile Sterivex filter was used for each
310   DNeasy PowerWater Sterivex kit to account for possible kit contamination. The thermal cycler program
311   for all reactions began with an initial denaturation temperature of 98°C for 30 seconds, followed by 35
312   cycles of 98°C for 10 seconds, 60°C for 10 seconds, and 72°C for 15 seconds, followed by a final extension
313   of 72°C for 5 minutes. The samples were cleaned using the Agencourt AMPure PCR Purification Kit
314   (Beckman Coulter Life Sciences, Indianapolis, IN). The cleaned samples were sent to the University of
315   Rhode Island Genomics and Sequencing Center and sequenced on an Illumina MiSeq platform using the
316   Illumina MiSeq V3 chemistry at 2 x 300 cycles (NCBI BioProject PRJNA718862).

317

318   **2.5 Water mass analysis**

319   The water samples analyzed in this study were classified as a mixture of known water types defined
320   by their source water masses (SWM), whose physical and chemical characteristics have been well
321   documented (e.g., Tomczak, 1981). The SWM considered in this study were the Atlantic Water (AW),
322   Pacific Water (PW), Meteoric Water (MW), and Sea Ice Meltwater (SIM). To assess the contributions of

Biogeosciences
Discussions

EGU

323 these SWM to the mixed water samples, we employed a simple 4-endmember mass balance analysis
324 (Östlund and Hut, 1984) (see Fig. S1). This method assumes that the mixing processes between the waters
325 are linear, that the water tracer properties are conservative, i.e., they are not subject to any chemical or
326 physical alteration during mixing. The 4-endmember mass balance method was used to estimate the
327 fractional contribution of each end member (f_i) to the mixed water samples at each measured point. The f_i
328 values indicate the amount of each source water mass present in the given sample as described by Pardo et
329 al. (2012) and Newton et al. (2013).

330

331 $$f_{AW}+f_{PW}+f_{MW}+f_{SIM}=1$$
332 $$f_{AW}(SA)+f_{PW}(SA)+f_{MW}(SA)+f_{SIM}(SA)=SA_{obs}$$

333 $$f_{AW}(ANP)+f_{PW}(ANP)+f_{MW}(ANP)+f_{SIM}(ANP)=ANP_{obs}$$

334 $$f_{AW}(\delta^{18}O)+f_{PW}(\delta^{18}O)+f_{MW}(\delta^{18}O)+f_{SIM}(\delta^{18}O)=\delta^{18}O_{obs}$$

335

336 To constrain the mixing calculation, we used conservative tracers' absolute salinity (SA), $\delta^{18}O$, and an N:P-
337 based tracer (ANP) (Jones et al., 1998). The $\delta^{18}O$ was measured using a Picarro l2130-I CRDS water isotope
338 analyzer (University of Illinois at Chicago) with a wire mesh inserted in the vaporizer inlet to trap salt from
339 the seawater (doi: 10.1594/PANGEA.937538). The ANP ratio is a quasi-conservative water-mass tracers,
340 which allowed us to identify the contributions of different water masses in the mixing layers. Specifically,
341 we employed a four-component linear endmember mixing model using nutrients. Past studies have used
342 nutrients in their Redfield ratios to distinguish between Pacific and Atlantic-derived waters (Ekwurzel et
343 al., 2001; Whitmore et al., 2020). We calculated the Arctic Nitrate-Phosphate tracer (ANP) following the
344 method described by Newton et al. (2013).
345 *Arctic Nitrate-Phosphate tracer* – ANP was determined using Euclidean geometry by calculating
346 the distance between the sample and the trendlines for the Pacific and Atlantic, as shown in equations 3
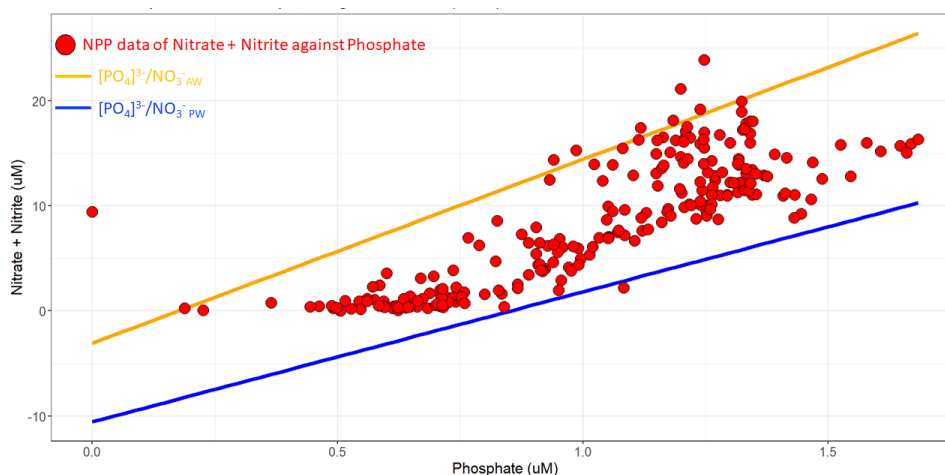347 and 4 (Jones et al., 1998; Whitmore et al., 2020 – Fig. 3).

348

349 $$NO_3^-{}_{AW} = (17.499 * [PO_4]^{3-}) - 3.072 \tag{1}$$

350 $$NO_3^-{}_{PW} = (12.368 * [PO_4]^{3-}) - 10.549 \tag{2}$$

351 $$ANP_{AW} = \frac{abs(5.6-17.499*0.2+3.072)}{sqrt(1^2)+(7.499^2)} \tag{3}$$

352 $$ANP_{PW} = \frac{abs(5.6-12.368*0.2+10.549)}{sqrt(1^2)+(12.368^2)} \tag{4}$$

353

354

Figure 3: Nitrate-Phosphate relationships, utilizing the Jones 1998 model and incorporating data (represented by red dots). The orange line represents $[PO_4]^{3-}$ / $NO_3^-{}_{AW}$ for Atlantic waters, while the blue line is $[PO_4]^{3-}$ / $NO_3^-{}_{PW}$ for Pacific waters.

ANP is a modified version of the N* tracer that considers the specific N:P ratios of the Arctic water column and is adjusted to the dynamic range of the pelagic Arctic Ocean (Newton et al., 2013). Unlike Redfield ratios, ANP can be influenced by processes other than photosynthesis and respiration. Bacterial nitrification and denitrification, which mainly occur in anoxic regions of the continental shelf benthos, can cause deviations from Redfield ratios (Newton et al., 2013). Therefore, ANP is well-suited for our dataset. We determined the concentrations of phosphate, and nitrate+nitrite using a Quik Chem Series 8500 Lachat analyzer (Serial Number 061100000379 – Hach, Loveland, Colorado, USA) with a heater configuration of 500 W Max. Reagents and standards were prepared using Quik Chem Protocols: Nitrate + Nitrite 31-107-04-1 A, Phosphate 31-115-01-1 H. To ensure the quality of the nutrient data, we first excluded data showing a standard deviation greater than 5% between replicated measurements. We then compared our dataset to literature values (e.g., Torres-Valdés et al., 2013; Bhatia et al., 2021) and data storage (e.g., DiTullio and Lee, 2019) to further verify the accuracy of our measurements. A flag value of 1 was assigned to the nutrient values that showed agreement with the reference data, indicating reliable data. We also attempted to identify outliers using N:P:Si ratios to achieve Redfieldian consistency, but this approach was not suitable for our dataset due to the significant impact of denitrification in shaping nutrient ratios in Pacific waters and the influence of freshwater inputs on nutrient utilization (e.g., Sterner and Elser, 2002). Other outlier identification procedures were also not effective for our dataset. The methods and sources for selecting endmembers were carefully chosen to ensure the accuracy and reliability of the calculated fractions. The study's DOI for further reference is 10.18739/A2BN9X45M.

End Member determination - The selection of endmembers was based on the data from the study and previous literature (Table 1). The salinity endmembers included data from the study for Atlantic Water (AW) and Pacific Water (PW) and values from literature for Meteoric Water (MW) and Sea Ice Meltwater (SIM) (Ekwurz et al., 2001; Newton et al., 2013; Whitmore et al., 2020). For ANP, the values for AW, PW, and MW were adopted from Newton et al. (2013), while the upper 50m values of SIM were used. For $\delta^{18}O$,

383   end member values from the study for AW and PW were utilized, along with a value of -20 ‰ for MW
384   from Whitmore et al. (2020) and surface values of +2.6 ‰ for SIM from Newton et al. (2013).

385   Table 1: MP endmembers. AW, PW, MW, SIM are the source water masses (SWMs); SA is the absolute S
386   (g/kg), ANP is the Arctic nitrate-phosphate tracer, MB is the mass balance; $\delta^{18}O$ was measured in ‰. For
387   SIM, the ANP and $\delta^{18}O$ tracers were calculated as averaged surface values per each CTD station; for $\delta^{18}O$
388   tracer, we also added 2.6 ‰ as in Newton et al., (2013).

389

	AW	PW	MW	SIM
SA (g/kg)	34.50	32.50	0	4
ANP	0	1	0	Surface values
$\delta^{18}O$ (‰)	0	-2.50	-20	Surface values + 2.6
MB	1	1	1	1

390

391   All the tracers were standardized as follows:

$$\frac{data - mean(data)}{SD(data)}$$

392

393   as they were measured in different measurement units (Table 1). Standardization gives each tracer a similar
394   dynamic range and equivalent weighting in the least squares calculation. The mass balance constraint was
395   assigned a higher weight to ensure all water mass fractions would sum to 1. To avoid interpreting samples
396   that do not conform to the linear mixing model, we adopted the criteria that the mass fractions cannot
397   deviate by more than 5% from the constraint of 1 (Tomzak, 1981; Tomczak and Large, 1989). The error
398   for every endmember was calculated as follows:

399                                    $$a = fi * endmember(obs)$$

400 $$b = sum(a)$$

401                    $$error = \left(\frac{endmember(obs) - b}{endmember(obs)}\right) * 100$$

402   Where *fi* is the water mass fraction for every SWM.

403   Any samples not conforming to this criterion was excluded from the water mass analysis (see Figure S2).

404

405   **3. Results**
406

3.1 Dissolved in-situ methane concentration and isotopic ratio

Overall, the range of methane concentrations values varied between 1.35 and 16.38 nM across the entire dataset, whereas the isotopic ratio varied between -64.2 and -17 ‰, with lowest isotope ratios in the surface ocean. The average of the $[CH_4]$ was 4.17 ± 2.5 nM, and the values below the average were recorded within deeper layers (av. depth = 190m). The supersaturation of methane in seawater relative to atmospheric methane concentrations (average 3.42 ± 0.05 nM) in the CAA varied spatially due to variations in temperature and salinity. In the surface waters (down to ~40 m depth), the saturation of CH_4 was mostly above equilibrium, with a maximum of methane saturation anomaly of ~ 360%, while in deeper layers, the methane saturation anomaly was mostly negative (Fig. 4). The negative correlation (-0.56 of Spearman's rank correlation coefficient, Fig. S8) between CH_4 and salinity (Fig. S3) corroborated that freshwater was associated with higher $[CH_4]$. According to Figure 4, the methane enrichment and depletion across a longitudinal scale did not show a clear trend.
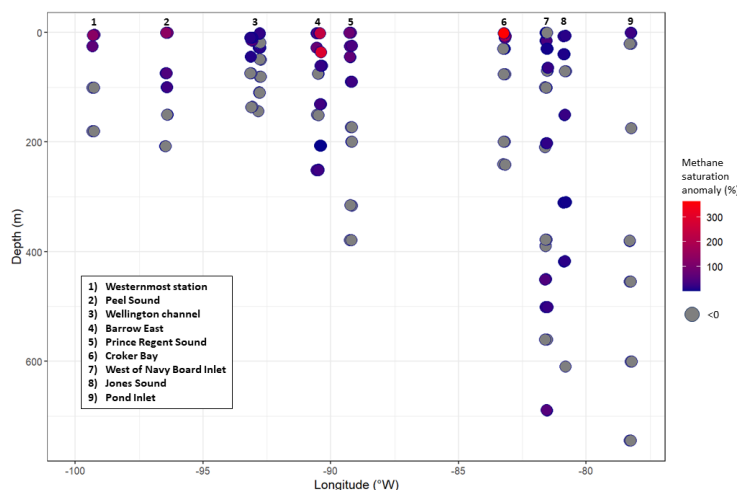
Figure 4: Methane saturation anomaly (%) across the longitudinal scale. The grey dots represent methane depletion (sat. anomaly <0%).

The entire data set showed an inverse correlation (-0.50 of Spearman's rank correlation coefficient, Fig. S8) between methane concentration and isotope ratio (Figure 5). At the low range of concentrations, the variability in $\delta^{13}CH_4$ becomes quite large, suggesting the potential for a variety of inputs. In Figure 5, we showed the methane oxidation curve calculated using a Rayleigh distillation model with initial concentration and isotope ratio corresponding to an approximate hypothetical initial condition of $\delta^{13}CH_4 =$ -63 and $[CH_4] = 15$ nM, as well as a kinetic isotope fractionation factor of 1.025 (Kendall and Caldwell, 1998; Fenwick et al., 2017). Rayleigh distillation model assumes that isotopic fractionation during methane degradation occurs because of the preferential removal of the lighter isotope, ^{12}C, over the heavier isotope, ^{13}C. As the degradation proceeds, the remaining methane becomes progressively enriched in the heavier isotope, resulting in a depletion of the lighter isotope.
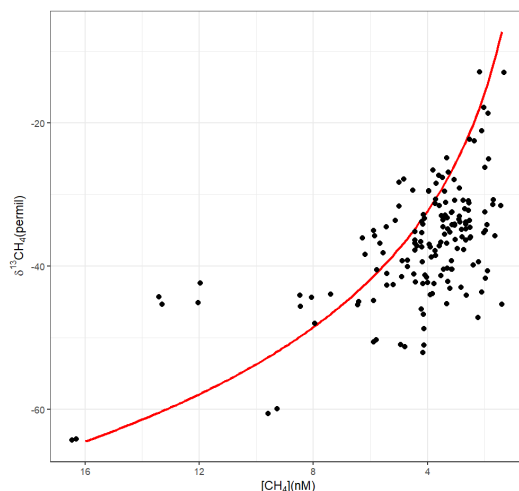
Figure 5: Methane oxidation curve calculated using a Rayleigh distillation model, with an initial concentration of 15 nM, a $\delta^{13}CH_4$ value of -63 ‰, and an isotopic fractionation factor of 1.025. The red line describes the Rayleigh curve. The curve shows the relationship between the remaining methane concentration and the corresponding isotopic composition of the remaining methane. The slope of the Rayleigh curve represents the isotopic fractionation factor, which is a measure of the degree of isotopic fractionation that occurs during the degradation of methane.

Figures 6 a and b show the discrete methane profiles of isotope ratio (a) and concentration coupled with the methane concentration at the atmospheric equilibrium (b) in Croker Bay. All the in-situ methane profiles can be found in Figure S4. Croker Bay represented the site with the highest supply of meltwater (mainly meteoric origin, MW) and recorded the highest methane concentration (Fig. 6b, ~17nM) coupled to the lowest isotopic signature (Fig. 6a, ~-64.3 ‰). In Croker Bay, the subsurface [CH_4] was close to atmospheric equilibrium, while concentrations were higher in the upper 25 m (Fig. 6b). West of Navy Board Inlet was the only site showing deep water methane enrichment (see Fig. S4), with an average of 3.4±0.03 nM in waters below 100m.
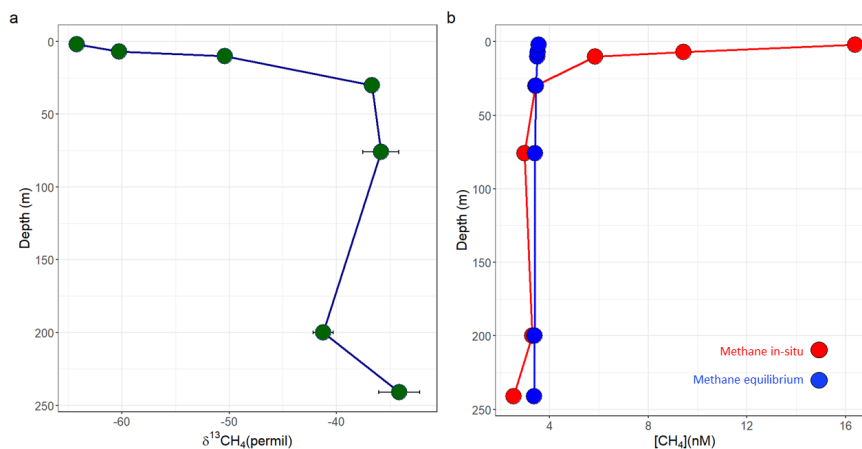
453

454 Figure 6: Methane data from samples collected in Croker Bay. a) methane isotope ratio profile; b) in-situ
455 methane concentration and methane concentration at the equilibrium relative to the atmosphere capacity
456 (methane equilibrium).

457

458   In summary, the in-situ methane concentration and isotopic ratio showed overall methane excess
459 in the upper 200 m of the water column (Figs 6 and S4), suggesting methane production in shallow waters
460 and methane uptake in deeper waters during the past.

461

462 **3.2 In-vitro methane oxidation potential**
463   The microbial oxidation rates (r_{ox}) with rate constants (k_{ox}) were calculated as in Uhlig and Loose
464 (2017), and the averaged values, per site and depth, are shown in Table 2.

465

466 Table 2: Methane oxidation rate constant (k_{ox}) averaged per site and depth ($k_{ox}.av$ (d^{-1})), and the associated
467 microbial methane oxidation rates (r_{ox} (nM/d)). In the table we also show the location (Site) and the depth
468 of the sample collected; moreover, we show the standard deviation between the averaged k_{ox} ($k_{ox}.SD$).
469

Site	Depth	$k_{ox}.av$ (d^{-1})	$k_{ox}.SD$	r_{ox} (nM/d)
JS	609	0.005	0.005	0.997
JS	7	0.003	0.001	0.458
WNBI	70	0.007	0.005	4.040
WNBI	15	0.005	0.001	2.000
WNBI	450	0.006	0.001	2.700
WNBI	70	0.004	0.002	1.030
WNBI	743	0.003	0.002	1.530
WNBI	401	0.000	0.000	0.000
WC	10	0.009	0.002	2.600
PRS	25	0.000	0.000	0.000
CB	241	0.008	0.008	0.760

|				
CB	7	0.009	0.004	2.200

470

471 In total, 83% of in-vitro samples exhibited significant methane oxidation, while the remaining 17% revealed
472 negligible or insignificant metabolic activity with respect to methane.

473   In Figure 7, we showed the vertical distribution of the methane oxidation rate constant (k_{ox}). The
474 vertical trend of the methane oxidation rates showed widespread oxidation potential for methane (positive
475 k_{ox}), with highest values within WC and CB shallow waters, reaching up to 0.01 d^{-1}. During the in-vitro
476 experiments, we recorded flat trend of methane concentrations and isotope ratio over time in two samples
477 (shown by grey dots in Fig.7), suggesting no methane metabolism. We did not take these values into account
478 for the microbial methane oxidation rate assessment, to not bias the results.

479
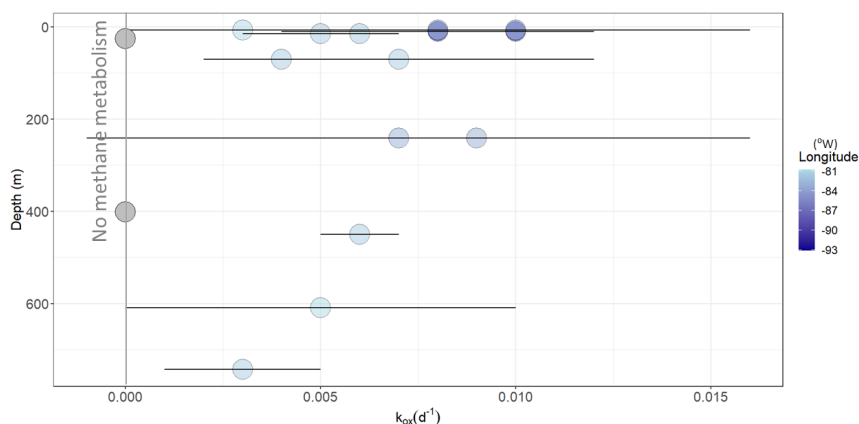
480
481 Figure 7: Vertical profiles of methane oxidation rate constant (k_{ox}) colored by longitude. The dots represent
482 all the k_{ox} values, while the horizontal lines indicate the standard error of the averaged k_{ox} values between
483 $k_{ox.mass.balance}$ and $k_{ox.isotope.ratio}$. The grey dots represent samples exhibiting no methane metabolism.

484

485   The methane oxidation rate constant results (k_{ox}) indicate a spatial trend across the study area, with
486 the potential for the highest oxidation rates observed towards the western Channel. This trend is visually
487 represented in Figure 7 through a color-coded longitudinal scale, where the darker blue dots matched with
488 higher k_{ox} values.

489   In summary, our findings reveal both spatial and vertical gradients within the water column, with
490 the highest k_{ox} values recorded towards the west, descending to a depth of 200m, followed by a gradual
491 decrease towards the east (as represented by the light blue dots in Figure 7). Overall, the waters of the CAA
492 exhibited a potential oxidative environment, in the summer of 2019, where in-situ methane excess could
493 have served as food source for methane oxidizers. The oxidation detection limit was passed between 5 and
494 18 incubation days after incubation began, revealing the range of rates we observed.

495

496 **3.3 Microbial community composition**
497 The 16S rRNA gene analysis of the in-situ water column community revealed phylogenetic diversity. The
498 in-situ microbial community structure was dominated by Flavobacteriaceae, including *Polaribacter sp.*

499 (Gonzalez et al., 2008), which are known to be heterotrophic, psychrophilic, and mesophilic. Following the
500 incubation period, most of the 16S rRNA gene sequences clustered into operational taxonomic units (OTUs)
501 affiliated with Alphaproteobacteria, Gammaproteobacteria, and Flavobacteriaceae (Bacteroidetes). The
502 dominant taxa observed in samples displaying methane oxidation were *Oleispira* (γ-proteobacteria),
503 *Planctomarina* (α-proteobacteria), and *Aurantivirga* (flavobacteria, Song et al., 2015). While
504 Alphaproteobacteria and Gammaproteobacteria include known methane-oxidizing bacteria, *Oleispira* and
505 *Planctomarina* are not yet classified as such. However, these taxa were also found in Arctic methane
506 incubations by Uhlig et al. (2018) and Gründger et al. (2021), suggesting their association with methane
507 oxidation. Flavobacteria are typically secondary consumers of methane, oil, or cellular decay products (e.g.,
508 Radajewski et al., 2002; Jensen et al., 2008; Redmond and Valentin, 2011). While methane oxidizers have
509 limited ability to consume multi-carbon substrates (Hanson & Hanson, 1996), many oil degraders cannot
510 consume methane (Rojo, 2009). Flavobacteria are often associated with the degradation of high molecular
511 weight dissolved organic carbon compounds (Cottrell and Kirchman, 2000), which may coincidentally be
512 associated with methane uptake. In summary, our dataset highlights the occurrence of Chloroplast genomes,
513 *Oleispira*, *Planctomarina*, and *Aurantivirga* in samples showing potential methane oxidation, consistent
514 with the findings of Uhlig et al. (2018) and Gründger et al. (2021).
515

516 **3.4 Dissolved methane and isotope ratio in sea ice**
517 Methane dissolved in sea ice was in the range of 3.4 and 21.2 nM (Fig. S5), showing concentrations
518 higher than in seawater ([CH$_4$] max in CB = 16.4 nM). On average, the sea ice recorded [CH$_4$] of 9.2 ± 5
519 nM, while seawater showed an average of 4 ± 2 nM. The methane maximum was recorded within
520 Westernmost Station sea ice core (21 nM), however, all the samples exhibited methane oversaturation with
521 respect to the atmospheric concentration (av. 4.7 ± 0.01 nM) above the bottom. Core 1 at the surface and
522 Core 2 at the bottom showed methane depletion (3.4 and 4.1 nM, respectively) (Fig. 8). Both these cores
523 were characterized by thicker multi-year ice (Canadian Ice Service and Table S2) and were collected in the
524 vicinity of Westernmost Station.
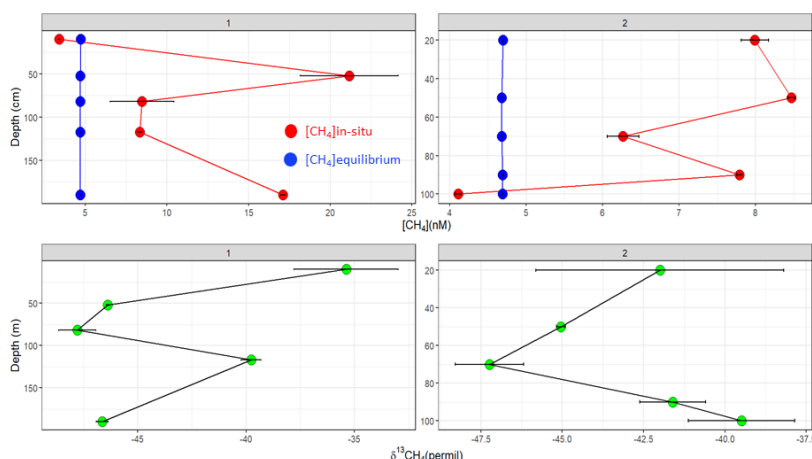
525

526 Figure 8: Methane concentrations and isotope ratios along the vertical profiles within sea ice. The red dots
527 indicated the in-situ methane concentrations along the sea ice core, with the methane concentrations at the

528   equilibrium relative to the atmosphere capacity (blue dots). The green dots showed the isotope ratio
529   ($\delta^{13}CH_4$) of cores 1 and 2. The headers displayed the core numbers as exhibited in Fig.1.
530

531   Cores 3, 4, and 5 were collected respectively in Peel Sound, close to Cunningham River, and in
532   Prince Regent Sound (see Fig.1), and they were characterized by first-year ice (Canadian Ice Service).
533   There was no trend of methane concentrations from first-year to multi-year ice, hence from west to east
534   (Fig. S6). The $\delta^{13}C$ isotopic signature in sea ice cores was between -51.4 and -35.4 ‰, showing less
535   variability in comparison to the in-situ water samples data.

536

537   **3.5 [CH₄] and k$_{ox}$ in relation to water masses.**
538   Dissolved methane was inversely correlated to AW (-0.4 Spearman's rank correlation coefficient)
539   and positively correlated with PW (0.3 Spearman's rank correlation coefficient) (Fig. 9 a and b), while the
540   data showed positive correlation with meteoric and sea ice meltwaters (0.44 and 0.37, respectively) (Fig. 9
541   c and d). Similarly, methane oxidation was weakly anticorrelated with AW (-0.17 Spearman's rank
542   correlation coefficient) (Fig. 9 e), and positively correlated with PW (0.17 Spearman's rank correlation
543   coefficient) (Fig. 9 f). The meltwaters exhibited a positive correlation with k$_{ox}$, as depicted in Figure 9 g
544   and h, with meteoric waters showing the highest Spearman's rank correlation coefficient of 0.76 (Fig. 9 g).
545   Spearman's matrices were separately computed for the in-situ and in-vitro data due to the limited availability
546   of the latter, resulting in fewer data points in Figure 9 e, f, g, and h.

547

548
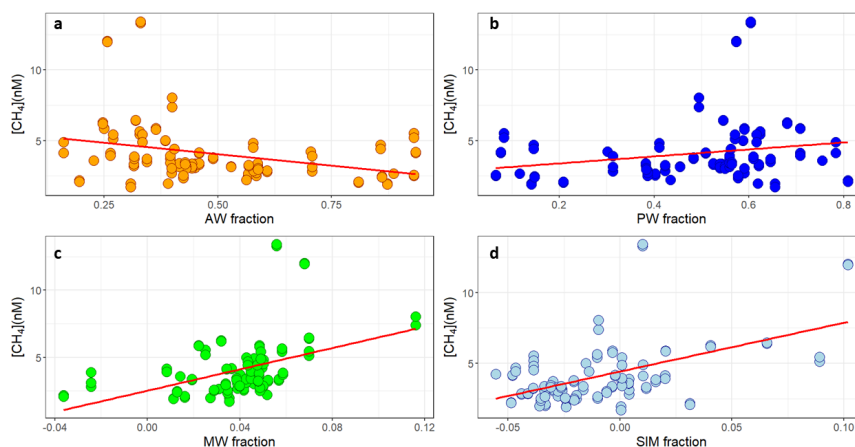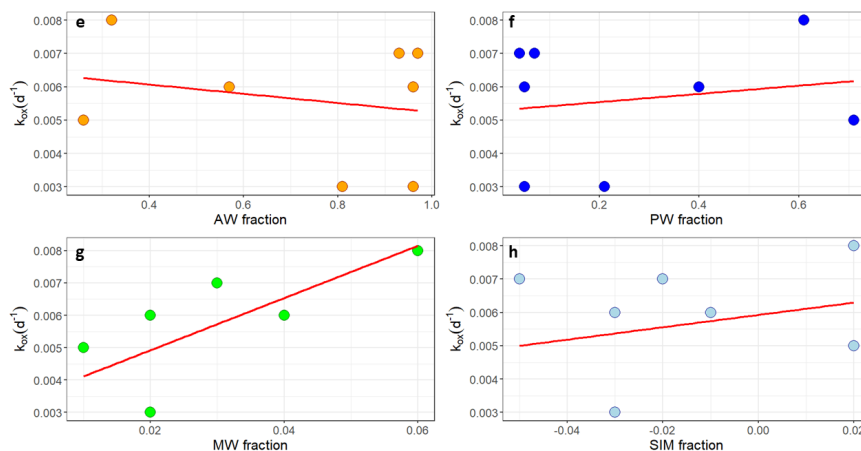
549
Figure 9: The correlation between methane concentrations measured in situ and the methane oxidation rate constant (k_{ox}) was examined in relation to water mass fractions. Panels a, b, c, and d illustrate the methane concentrations measured in situ in relation to Atlantic and Pacific waters (a and b) as well as meltwater masses (c and d). Panels e, f, g, and h depict the methane oxidation rate constant in relation to Atlantic and Pacific waters (e and f) and the meltwaters (g and h). It should be noted that the results for the meltwaters may potentially increase, as they do not include the meteoric supply from Devon Ice Cap.

Summarizing, the analysis revealed the presence of two distinct environments with regards to methane activity. One environment exhibited active methane metabolism, while the other displayed non-metabolic behavior towards methane. This differentiation led to a distinct distribution of methane oxidation rates across the study area, as depicted in Figure 10. In the Atlantic water regime, dissolved methane was depleted with concentrations below the equilibrium saturation range, where we also recorded weaker methane microbial metabolism. The occurrence of no detectable methane oxidation in the deep layers of West Navy Board Inlet and in shallow Prince Regent Sound waters was not associated to unique thermohaline characteristics of the two sites, and unfortunately, the community structure was not analyzed in those sites.
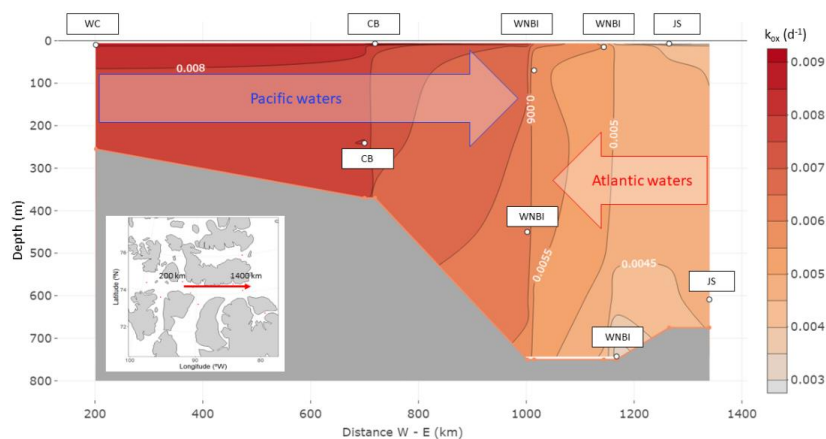
Figure 10: Parry Channel segment with color-coded k_{ox} averages by transect and depth, Excluding non-methane metabolism data (selected $k_{ox}>0$). Arrows Indicate Atlantic Water (AW) and Pacific Water (PW) intrusion into the Channel. White dots represent data points, with location details displayed in text boxes above. The x-axis measures distances (in km) from Wellington Channel (longitude = 93.11°W), 200 km away, to the Easternmost Point (longitude = 78.26°W), spanning 1400 km. Refer to the map in the lower left corner for further details.

4. Discussion

In the waters of the Canadian Arctic Archipelago, dissolved methane showed the strongest variations vertically in the water column, with higher concentrations detected in shallow waters. This distribution pattern suggests an influence of the water column structure on methane concentrations. The water column structure in the CAA was characterized by a seasonal meltwater mixed with Pacific Water (PW), overlying layers of PW and Atlantic Water (AW). Pacific Water was found to comprise more than 50% of the water above 200 m (Fig. S1), which correlated with areas of highest methane oxidation. The vertical distribution of methane concentrations was evident through various indicators. In addition to the positive correlation with PW and negative correlation with AW (Section 3.5), methane concentrations and absolute salinity (SA) were strongly correlated (Figure S3). Additionally, the Pearson correlation coefficient between them was -0.56, further supporting this relationship. Similarly, the potential methane oxidation rate exhibited a vertical profile, with higher values found in shallow waters. This pattern was also supported by a negative correlation with SA (R=-0.47). Conversely, lower oxidation rates were observed in samples collected from deeper layers, indicating that the AW-origin layers did not support potential methane microbial metabolism. The hydrographic context of these findings provides valuable insights into the main drivers of methane metabolism during the summer in this specific Arctic region. The relatively weak oxidation rates in near-bottom waters and indeed throughout the subsurface distribution of AW (see Fig. 10), did not suggest subsurface inputs of methane such as cold seeps, nor any strong role for AW in the methane cycle within the CAA. Previous research conducted near methane sources, such as Arctic shelf gas seeps, has shown that seasonal variations of water masses can affect methane oxidation rates, resulting in system-wide changes in the efficiency of water column methane oxidizers (Steinle et al., 2015, 2017; Gründger et al., 2021).

19

597   Instead, the distribution of k_{ox} and [CH_4] suggest a connection between methane cycling (both
598   production and consumption) in near-surface waters. Potential explanations include the possibility of
599   methane production within phosphate-limited PW (Repeta et al., 2016), methane production associated with
600   breakdown of primary products such as DMSP (Damm et al., 2015 and 2008), or methane production
601   associated with terrestrial freshwater in rivers (Manning et al., 2020 and 2022) or from glaciers (Pain et al.,
602   2021). We explore each of these possible explanations in the sections that follows.
603
604   **4.1 Possible sources of dissolved methane**
605   Overall, the dissolved methane in-situ suggested a water column that is strongly affected by
606   methane oxidation to first order (see Fig. 5), but the large scatter of isotopic ratios, especially at low methane
607   concentrations also suggests multiple sources in an open system as the area of study. The highest dissolved
608   methane concentrations were recorded in shallow meltwaters mixed with PW, concurrently with the lowest
609   nutrient supply and high chlorophyll-a fluorescence data (e.g., Westernmost Station and Prince Regent
610   Sound). More recently, several methanogenesis metabolism pathways have been identified that may
611   produce CH_4 in situ in the surface ocean mixed layer, providing a more direct conduit to the atmosphere
612   (Karl et al., 2008; Lenhart et al., 2016; Schmale et al., 2018).
613   The highest dissolved methane concentrations (>5 nM) were observed in the western CAA (with
614   longitudes greater than or equal to 90 degrees west), except for Crocker Bay (av. [CH_4]=12.9 nM). Croker
615   Bay was not representative of the eastern Channel either, due to its influence from the Devon Ice Cap
616   drainage. The highest values were recorded in: Barrow East ([CH_4]$_{av}$ = 10.53 nM), Peel Sound ([CH_4]$_{av}$ =
617   8.5 nM), Westernmost Station ([CH_4]$_{av}$ = 7.7 nM), and Prince Regent Sound ([CH_4]$_{av}$ = 6.4 nM). Barrow
618   East and Peel Sound waters were characterized by high freshwater supply (Fig. S1) provided by
619   Cunningham and Garnier Rivers (McLaughlin et al., 2014) and watershed drainage of marine-terminating
620   rivers from the southern Canadian Arctic Archipelago, respectively (Brown et al., 2020). All sites were
621   distinguished by substantial meltwater input (with meteoric water and sea ice meltwater exceeding 10%,
622   Fig. S1) and anticipated detrital organic matter supply, which supports the hypothesis that methanogenesis
623   occurred in the past and was influenced by particle supply within the water masses. Notably,
624   methanogenesis in terrestrial fluvial systems and beneath terrestrial glaciers could explain the high marine
625   methane concentrations observed at these sites (Valentine et al., 1994; Bange et al., 2010). Furthermore,
626   the isotopic signature of methane in shallow Croker Bay waters reached values lower than -64‰ (very
627   depleted in $\delta^{13}C$), suggesting subglacial methanogenesis from the Devon Ice Cap runoff (Pain et al., 2021).
628   The only site showing methane excess in deep waters (at 690 m depth) was West Navy Board Inlet, and we
629   recorded the methane maxima concurrently with relatively high turbidity (0.005 NTU). This outcome likely
630   suggested methane release from sediments (Damm et al., 2005; Graves et al., 2015; Silyakova et al., 2020).
631   The positive correlation between [CH_4] and SIM (Fig. 9) suggested that the sea ice melt cycle may
632   somehow play a role in seasonal methane production, and indeed elevated methane in ice cores could
633   suggest sea ice melt is a methane source, or the same mechanism that produces methane in sea ice is also
634   active in the water column. The Western CAA contained the greatest sea ice cover (see the sea ice
635   concentration in Fig. 11), mostly as multi-year ice (Canadian Ice Service). However, due to the warm
636   season, the sea ice also occurred in the form of permeable sea ice and sea ice meltwater. Notably, the
637   satellite-derived sea ice cover (Spreen et al., 2008) and the water mass estimates of sea ice meltwater tended
638   to coincide with greatest contributions in the West, with >10% occupying the water volume.
639   As described earlier, the sea ice cores showed higher dissolved methane than seawater, and the
640   western waters were methane enriched. This outcome suggested that the methane excess in the sea ice was

641 due to past freezing processes and that the increase of ice permeability influenced the methane enrichment
642 within the underneath seawater. Comparing our results with the ones from previous studies in the same
643 location in July 2005 (Kitidis et al., 2010), sea ice similarly influenced the methane oxidation rates. Our
644 outcome, confirmed by previous studies conducted in Utqiagvik (Loose et al., 2011) and the Central Arctic
645 (Damm et al., 2015; Damm et al., 2018), suggested that the residence time of methane gas in sea ice could
646 allow it to accumulate during the freezing period and be released during the melt period, supporting the
647 metabolic consumption in Sea Ice Meltwater. Verdugo et al. (2021) and Damm et al. (2015) described how
648 increased ice permeability at the ice bottom triggers methane release, causing low methane concentrations
649 at the bottom of the ice and methane enrichment in the water underneath. This process was well described
650 by the methane concentration in Core 2 (collected close to the Westernmost station). Here, the sea ice
651 enriched in methane could have released the gas and the relict detritus, favoring the conditions for microbial
652 methane production, explaining the methane excess in the waters underneath. The same condition, but
653 backwards, was recorded in Core 1, where we recorded sea ice oversaturated in methane, with the top
654 centimeters showing methane deficit. The methane initially entrapped in the sea ice was probably released
655 into the atmosphere when the sea ice surface became permeable (Verdugo et al., 2021). The in-situ
656 dissolved methane was distributed across the surface CAA waters mainly within meltwaters (see Fig. S1
657 and S4), without showing any clear relationship with sea ice concentration (Fig. 11), however logistical
658 constraints prevented the expedition from transiting very far through ice-covered regions, so this
659 relationship was difficult to establish.

660
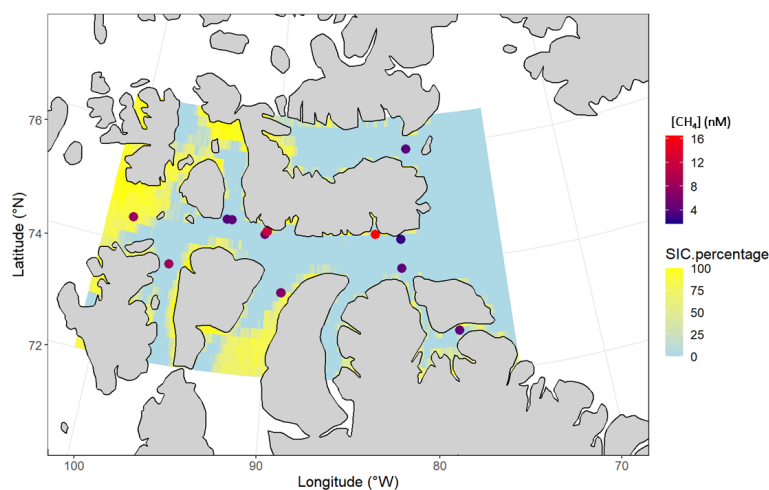
661
662 Figure 11: top view maps of the study area, with raster plots of the sea ice concentrations. The dots show
663 the [CH₄] recorded within the upper 100m of the water column. The upper color scale shows the methane
664 data, while the lower color code represents the Sea Ice Concentration in percentage.

665

666 In conclusion, we can state that the marine methane in the CAA was defined by two different
667 environments during the summer of 2019, partly influenced by the sea ice melting. In the past, other studies
668 showed the correlation between the sea ice and the greenhouse gases in the Arctic Ocean during the summer
669 (Damm et al., 2018, Verdugo et al., 2021), however, no data were yet referred to our study area.

670   To summarize, it is likely that dissolved methane in the CAA waters during the summer is primarily
671 driven by microbial metabolism, facilitated by the primary production and organic debris supplied by the
672 meltwaters (both meteoric and sea ice), with additional inputs from terrestrial or subglacial runoff.
673 However, the specific metabolic pathway for any aerobic methanogenesis remains unknown and was not
674 within the capabilities of this study to determine.
675

676 **4.2 Possible sources of methane oxidation potential**

677   Although we were unable to obtain incubation results from Westernmost Station, Barrow East, and
678 Peel Sound, we were able to observe the potential for microbial methane oxidation in Croker Bay, Prince
679 Regent Sound, and West Navy Board Inlet. Our incubation experiments at Croker Bay and West Navy
680 Board Inlet showed the potential for microbial methane oxidation in both surface and deeper layers (CB
681 average k_{ox} = 0.0085 d^{-1}, WNBI average k_{ox} = 0.0024 d^{-1}). This finding suggests that the excess methane
682 dissolved in the water column could be oxidized before reaching the atmosphere. Additionally, our
683 observations along the West Navy Board Inlet transect showed no detectable oxidation at 15m and 400m
684 depth, which, in conjunction with the low k_{ox} rates, suggested weak methane metabolism in waters above
685 the bottom layer. In Prince Regent Sound, we only analyzed one depth for methane oxidation rates (25 m)
686 and found no detectable oxidation potential. The results of genomic community composition analysis
687 revealed the occurrence of *Oleispira*, *Planctomarina*, and *Aurantivirga* in the "time final" samples, where
688 methane oxidation was detected. This finding suggested a potential linkage between these microorganisms
689 and methane uptake. In a previous study by Uhlig et al. (2018), *Oleispira* was found to be more abundant
690 in long-incubation samples than in situ samples, which were mainly dominated by α- and γ-proteobacteria.
691 In our study, after incubating the samples with methane standard, we observed a shift towards higher
692 fractions of α-proteobacteria, with *Planctomarina* being the dominant genus. The occurrence of *Oleispira*,
693 likely belonging to *Oleispira lenta* (Wang et al., 2012), and *Aurantivirga* taxa, highlighted the potential
694 influence of Pacific water in methane oxidation, as these taxa have been predominantly found in North
695 Pacific waters (Wang et al., 2012; Song et al., 2015). Notably, *Aurantivirga* occurred only in deeper layers,
696 indicating its association with *Aurantivirga profunda*, a species isolated from deep seawater (Song et al.,
697 2015).

698   The present study showed an average value of the oxidation rate constant (k_{ox}) of 0.006±0.002 d^{-1}
699 (excluding non-methane metabolism), which fell within the range of values reported in previous Arctic
700 research (e.g., Mau et al., 2017; Uhlig and Loose, 2017). The microbial oxidation rates (r_{ox}) reported in this
701 study also fell within the same range of values showing a good agreement with global methane data, as
702 depicted in Figure S7. In comparison, the only available data on methane oxidation in the Canadian Arctic
703 Archipelago waters was from 2005 (Kitidis et al., 2010) and reported significantly higher k_{ox} values
704 compared to other measurements in the Arctic, including those from seeps. The average k_{ox} reported by
705 Kitidis et al. (2010) was 0.09 d^{-1}. It is noteworthy that the oxidation rate measurements reported by Kitidis
706 et al. relied solely on methane mass balance, which can result in high oxidation rate anomalies if methane
707 gas leaks from the incubation chamber.

708   Our results indicated only a weak correlation between in-situ dissolved methane concentration and
709 methane oxidation potential (k_{ox}) (Spearman's rank correlation coefficient = 0.15, Fig. S9). However,
710 methane oxidation can be expected in waters with high methane concentrations that are oversaturated with
711 respect to atmospheric levels. Previous studies conducted in the Arctic and in cold seeps located on
712 continental slopes worldwide (Mau et al. 2013; Boetius & Wenzhöfer, 2013) have shown a positive
713 correlation between elevated methane oxidation activity and high dissolved CH_4 concentrations in marine

714 environments. These studies suggested that methane oxidizers may rapidly increase their oxidation rates in
715 response to the abundance of their food source. Our findings were not inconsistent with this thesis, as we
716 observed a relationship between methane oxidation and CH_4 concentrations in the CAA waters, however
717 the correlation was weak. While we acknowledge that the number of coupled in-situ and experimental
718 samples in our study was limited, the spatial coverage of our data is currently the most comprehensive
719 record of methane metabolism in these waters. Overall, methane oxidation rates showed direct correlation
720 with freshwater masses (Fig. 9), suggesting the influence of the CAA meltwater runoff on the methane
721 oxidizers.

722   In summary, we found weak or absent methane microbial oxidation in AW, while it was stronger
723 in meltwaters and PW. These results tend to support the role of surface processes in the CAA during the
724 summer, including input of meltwater, biology, and processes associated to the particulate organic matter.
725 While the dominant taxa associated with our methane oxidation process were not known methane oxidizers,
726 they have recently been connected to methane metabolism, highlighting the need for further investigation.
727

5. Conclusions

729   Collectively, the CAA waters showed methane oversaturation in the upper water column with
730 respect to atmospheric equilibrium saturation. The methane oversaturation was mainly associated with the
731 meltwaters, turbidity, and biology (in nutrient depleted environments), likely following one of the paths
732 explained by Repeta et al. (2016) and Sosa et al. (2020). In total, 83% of in-vitro samples were exhibited
733 significant methane oxidation, while the remaining 17% revealed negligible or insignificant metabolic
734 activity with respect to methane. The fastest oxidation rates were recorded within surface freshwater – both
735 sea ice melt and meteoric waters – as well as within Pacific-origin waters. The community structure likely
736 responsible for the methane oxidation was characterized by three main groups that have been recently
737 associated with the methane metabolism (*Aurantivirga, Oleispira and Planktomarina*); *Aurantivirga* and
738 *Oleispira* were both isolated from PWs. This outcome suggested that the PW predominance of the CAA
739 waters could have defined hotspots for methane oxidations. The sea ice melting also influenced the methane
740 distribution within the Sound, strengthening the hypothesis that the sea ice acted as a barrier for the gas
741 exchange during the former winter, releasing dissolved methane during the summer. The overall picture
742 suggested supersaturation of in-situ methane in shallow waters, coupled with faster oxidation rates in
743 meltwater and Pacific dominant layers, suggesting prevention of the methane migration into the atmosphere
744 towards the western CAA.

745   Summarizing, we can define the CAA waters into two different environments according to the
746 methane metabolism: a) methane-metabolic active and b) non-methane metabolic active. The west side of
747 the study area, including Croker Bay, showed great methane metabolism, where we had both in-situ
748 dissolved methane excess, and faster methane oxidation rates potential. The eastern side, including Jones
749 Sound and Pond Inlet data, characterized by Atlantic Water regime, exhibited lower methane concentrations
750 and oxidation rate constant. Due to the Atlantification of the Arctic Ocean (Polyakov et al., 2017, 2020),
751 we would expect higher intrusion of AW in the CAA at the expense of PW, with consequent sea ice melting.
752 This would exacerbate the stratification of the dissolved methane, enhancing isolated methane-associated
753 community.
754

755 **Data availability**

Biogeosciences
Discussions
EGU
Open Access

The produced database of this study has been archived in Arctic Data Center and can be assessed using the following link: https://doi.org/10.18739/A2BN9X45M. The sequence analysis and taxonomical classification is stored at National Center for Biotechnology Information (NCBI BioProject PRJNA718862).

Author contribution

B.L. designed the research. B.L. and A.D. implemented the study. A.D., C.G-E., Z.K., J.S., F.C., N.V., H.R., T.E., S.U., B.L., were involved in the sampling activities. A.D., B.L., N.V., H.R., T.E., S.U., performed the analysis. A.D., B.L., A.L.K., M.G-M., F.C., C.G-E. processed the data. A.D. and B.L. wrote the manuscript, with input from all authors.

Competing interests

The authors declare that they have no conflict of interest.

References

Agnew, T. and Howell, S.: The use of operational ice charts for evaluating passive microwave ice concentration data, Atmosphere - Ocean, 41, 317–331, https://doi.org/10.3137/ao.410405, 2003.

Alonso-Sáez, L., Galand, P. E., Casamayor, E. O., Pedrós-Alió, C., and Bertilsson, S.: High bicarbonate assimilation in the dark by Arctic bacteria, ISME Journal, 4, 1581–1590, https://doi.org/10.1038/ismej.2010.69, 2010.

Bange, H. W., Freing, A., Kock, A., & Löscher, C. R. Marine pathways to nitrous oxide. In Nitrous Oxide and Climate Change (1st ed., pp. 36–62). Routledge. https://doi.org/10.4324/9781849775113, 2010.

Bhatia, M. P., Waterman, S., Burgess, D. O., Williams, P. L., Bundy, R. M., Mellett, T., Roberts, M., and Bertrand, E. M.: Glaciers and Nutrients in the Canadian Arctic Archipelago Marine System, Global Biogeochem Cycles, 35, https://doi.org/10.1029/2021GB006976, 2021.

Boetius, A. and Wenzhöfer, F.: Seafloor oxygen consumption fuelled by methane from cold seeps, https://doi.org/10.1038/ngeo1926, 2013.

Brown, K. A., Williams, W. J., Carmack, E. C., Fiske, G., François, R., McLennan, D., and Peucker-Ehrenbrink, B.: Geochemistry of Small Canadian Arctic Rivers with Diverse Geological and Hydrological Settings, J Geophys Res Biogeosci, 125, https://doi.org/10.1029/2019JG005414, 2020.

Carmack, E. C., Yamamoto-Kawai, M., Haine, T. W. N., Bacon, S., Bluhm, B. A., Lique, C., Melling, H., Polyakov, I. v., Straneo, F., Timmermans, M. L., and Williams, W. J.: Freshwater and its role in the Arctic Marine System: Sources, disposition, storage, export, and physical and biogeochemical consequences in the Arctic and global oceans, https://doi.org/10.1002/2015JG003140, 2016.

Cottrell, M. T. and Kirchman, D. L.: Community Composition of Marine Bacterioplankton Determined by 16S rDNA Gene Clone Libraries and Fluorescence In Situ Hybridization, APPLIED AND ENVIRONMENTAL MICROBIOLOGY, 5116–5122 pp., 2000.

Damm, E., Bauch, D., Krumpen, T., Rabe, B., Korhonen, M., Vinogradova, E., and Uhlig, C.: The Transpolar Drift conveys methane from the Siberian Shelf to the central Arctic Ocean, Sci Rep, 8, https://doi.org/10.1038/s41598-018-22801-z, 2018.

Damm, E., Helmke, E., Thoms, S., Schauer, U., Nöthig, E., Bakker, K., Kiene, R. P., and Wegener, A.: Methane production in aerobic oligotrophic surface water in the central Arctic Ocean, Biogeosciences, 1099–1108 pp., 2010.

Damm, E., Kiene, R. P., Schwarz, J., Falck, E., and Dieckmann, G.: Methane cycling in Arctic shelf water and its relationship with phytoplankton biomass and DMSP, Mar Chem, 109, 45–59, https://doi.org/10.1016/j.marchem.2007.12.003, 2008.

Damm, E., Rudels, B., Schauer, U., Mau, S., and Dieckmann, G.: Methane excess in Arctic surface water-triggered by sea ice formation and melting, Sci Rep, 5, https://doi.org/10.1038/srep16179, 2015.

DiTullio G, Lee P. Dissolved nutrient concentrations, High Arctic Ocean, August-September 2018. Arctic Data Center. https://doi.org/10.18739/A2CN6Z03F, 2019.

819   Dunbar, Moira. "The Geographical Position of the North Water." *Arctic* 22: 438-441,
820   DOI:10.14430/ARCTIC3235 Corpus ID: 129164760, 1969.

821   Ekwurzel, B., Schlosser, P., Mortlock, R. A., Fairbanks, R. G., and Swift, J. H.: River runoff, sea ice
822   meltwater, and Pacific water distribution and mean residence times in the Arctic Ocean, J GEOPHYS
823   RES-OCEANS, 106, 9075–9092, https://doi.org/10.1029/1999jc000024, 2001.

824   Fenwick, L., Capelle, D., Damm, E., Zimmermann, S., Williams, W. J., Vagle, S., and Tortell, P. D.:
825   Methane and nitrous oxide distributions across the North American Arctic Ocean during summer, 2015,
826   J Geophys Res Oceans, 122, 390–412, https://doi.org/10.1002/2016JC012493, 2017.

827   Ferré, B., Jansson, P. G., Moser, M., Serov, P., Portnov, A., Graves, C. A., Panieri, G., Gründger, F.,
828   Berndt, C., Lehmann, M. F., and Niemann, H.: Reduced methane seepage from Arctic sediments during
829   cold bottom-water conditions, Nat Geosci, 13, 144–148, https://doi.org/10.1038/s41561-019-0515-3,
830   2020.

831   Fisher, R. E., Sriskantharajah, S., Lowry, D., Lanoisellé, M., Fowler, C. M. R., James, R. H.,
832   Hermansen, O., Lund Myhre, C., Stohl, A., Greinert, J., Nisbet-Jones, P. B. R., Mienert, J., and Nisbet,
833   E. G.: Arctic methane sources: Isotopic evidence for atmospheric inputs, Geophys Res Lett, 38,
834   https://doi.org/10.1029/2011GL049319, 2011.

835   González JM, Fernández-Gómez B, Fernàndez-Guerra A, Gómez-Consarnau L, Sánchez O, Coll-Lladó
836   M, Del Campo J, Escudero L, Rodríguez-Martínez R, Alonso-Sáez L, Latasa M, Paulsen I,
837   Nedashkovskaya O, Lekunberri I, Pinhassi J, Pedrós-Alió C. Genome analysis of the proteorhodopsin-
838   containing marine bacterium Polaribacter sp. MED152 (Flavobacteria). Proc Natl Acad Sci U S A.
839   105(25):8724-9. doi: 10.1073/pnas.0712027105. Epub 2008 Jun 13. PMID: 18552178; PMCID:
840   PMC2438413, 2008.

841   Graves, C. A., L. Steinle, G. Rehder, H. Niemann, D. P. Connelly, D. Lowry,R. E. Fisher, A. W. Stott,
842   H. Sahling, andR. H. James. Fluxes and fate ofdissolved methane released at theseafloor at the landward
843   limit of thegas hydrate stability zone offshorewestern Svalbard, J. Geophys. Res.Oceans,120, 6185–
844   6201, doi:10.1002/2015JC011084, 2015.

845   Gründger, F., Probandt, D., Knittel, K., Carrier, V., Kalenitchenko, D., Silyakova, A., Serov, P., Ferré,
846   B., Svenning, M. M., and Niemann, H.: Seasonal shifts of microbial methane oxidation in Arctic shelf
847   waters above gas seeps, Limnol Oceanogr, 66, 1896–1914, https://doi.org/10.1002/lno.11731, 2021.

848   Hanson RS, Hanson TE. Methanotrophic bacteria. Microbiol Rev. 1996 Jun;60(2):439-71. doi:
849   10.1128/mr.60.2.439-471. PMID: 8801441; PMCID: PMC239451, 1996.

850   Ingram, R. G. and Larouche, P.: Variability of an under-ice river plume in Hudson Bay, J Geophys Res
851   Oceans, 92, 9541–9547, https://doi.org/10.1029/JC092iC09p09541, 1987.

852   Jensen, S., Neufeld, J. D., Birkeland, N. K., Hovland, M., and Murrell, J. C.: Methane assimilation and
853   trophic interactions with marine Methylomicrobium in deep-water coral reef sediment off the coast of
854   Norway, FEMS Microbiol Ecol, 66, 320–330, https://doi.org/10.1111/j.1574-6941.2008.00575.x,
855   2008.

856 Jones, E. P., Anderson, L. G., and Swift, J. H.: Distribution of Atlantic and Pacific waters in the upper
857 Arctic Ocean: implications for circulation, Geophys Res Lett, 25, 765–768,
858 https://doi.org/10.1029/98GL00464, 1998.

859 Kendall, C., & Caldwell, E.A. Fundamentals of Isotope Geochemistry, 1998.

860 Kerrigan Z, D'Hondt S. Patterns of Relative Bacterial Richness and Community Composition in
861 Seawater and Marine Sediment Are Robust for Both Operational Taxonomic Units and Amplicon
862 Sequence Variants. Front Microbiol. 13:796758. doi: 10.3389/fmicb.2022.796758. PMID: 35197949;
863 PMCID: PMC8859096, 2022.

864 Kitidis, V., Upstill-Goddard, R. C., and Anderson, L. G.: Methane and nitrous oxide in surface water
865 along the North-West Passage, Arctic Ocean, Mar Chem, 121, 80–86,
866 https://doi.org/10.1016/j.marchem.2010.03.006, 2010.

867 Loose, B., Schlosser, P., Perovich, D., Ringelberg, D., Ho, D. T., Takahashi, T., Richter-Menge, J.,
868 Reynolds, C. M., Mcgillis, W. R., and Tison, J. L.: Gas diffusion through columnar laboratory sea ice:
869 Implications for mixed-layer ventilation of CO2 in the seasonal ice zone, Tellus B Chem Phys
870 Meteorol, 63, 23–39, https://doi.org/10.1111/j.1600-0889.2010.00506.x, 2011.

871 Ludwig, V., G. Spreen, & L. T. Pedersen. Evaluation of a New Merged Sea-Ice Concentration Dataset
872 at 1 km Resolution from Thermal Infrared and Passive Microwave Satellite Data in the Arctic. Remote
873 Sens. 12(19), 3183. doi:10.3390/rs12193183, 2020.

874 Ludwig, V., Spreen, G., Haas, C., Istomina, L., Kauker, F., and Murashkin, D.: The 2018 North
875 Greenland polynya observed by a newly introduced merged optical and passive microwave sea-ice
876 concentration dataset, The Cryosphere, 13, 2051-2073, doi:10.5194/tc-13-2051-2019, 2019.

877 Manning, C. C. M., Zheng, Z., Fenwick, L., McCulloch, R. D., Damm, E., Izett, R. W., et al. Interannual
878 variability in methane and nitrous oxide concentrations and sea-air fluxes across the North American
879 Arctic Ocean (2015–2019). Global Biogeochemical Cycles, 36, e2021GB007185.
880 https://doi.org/10.1029/2021GB007185, 2022.

881 Manning, C. C., Preston, V. L., Jones, S. F., Michel, A. P. M., Nicholson, D. P., Duke, P. J., et al. River
882 inflow dominates methane emissions in an Arctic coastal system. Geophysical Research Letters, 47,
883 e2020GL087669. https://doi.org/10.1029/2020GL087669, 2020.

884 Mau, S., Blees, J., Helmke, E., Niemann, H., and Damm, E.: Vertical distribution of methane oxidation
885 and methanotrophic response to elevated methane concentrations in stratified waters of the Arctic fjord
886 Storfjorden (Svalbard, Norway), Biogeosciences, 10, 6267–6268, https://doi.org/10.5194/bg-10-6267-
887 2013, 2013.

888 Mau, S., Römer, M., Torres, M. et al. Widespread methane seepage along the continental margin off
889 Svalbard - from Bjørnøya to Kongsfjorden. Sci Rep 7, 42997. https://doi.org/10.1038/srep42997, 2017.

890 Mclaughlin, F., Carmack, E., Proshutinsky, A., Krishfield, R. A., Guay, C., Yamamoto-Kawai, M.,
891 Jackson, J. M., and Williams, B.: The Rapid Response of the Canada Basin to Climate Forcing: FROM
892 BELLWETHER TO ALARM BELLS, Source: Oceanography, 24, 146–159,
893 https://doi.org/10.2307/24861309, 2007.

894   Newton, R., Schlosser, P., Mortlock, R., Swift, J., and MacDonald, R.: Canadian Basin freshwater
895   sources and changes: Results from the 2005 Arctic Ocean Section, J Geophys Res Oceans, 118, 2133–
896   2154, https://doi.org/10.1002/jgrc.20101, 2013.

897   Oh, Y., Zhuang, Q., Liu, L., Welp, L. R., Lau, M. C. Y., Onstott, T. C., Medvigy, D., Bruhwiler, L.,
898   Dlugokencky, E. J., Hugelius, G., D'Imperio, L., and Elberling, B.: Reduced net methane emissions
899   due to microbial methane oxidation in a warmer Arctic, Nat Clim Chang, 10, 317–321,
900   https://doi.org/10.1038/s41558-020-0734-z, 2020.

901   Östlund, H. G., and Hut, G. Arctic Ocean water mass balance from isotope data, J. Geophys. Res., 89(
902   C4), 6373– 6381, doi:10.1029/JC089iC04p06373, 1984.

903   Pachauri, R. K., Mayer, Leo., and Intergovernmental Panel on Climate Change: Climate change 2014 :
904   synthesis report, 151 pp., n.d.

905   Pain, A. J., Martin, J. B., Martin, E. E., Rennermalm, Å. K., and Rahman, S.: Heterogeneous CO2 and
906   CH4 content of glacial meltwater from the Greenland Ice Sheet and implications for subglacial carbon
907   processes, The Cryosphere, 15, 1627–1644, https://doi.org/10.5194/tc-15-1627-2021, 2021.

908   Pardo, P. C., Pérez, F. F., Velo, A., and Gilcoto, M.: Water masses distribution in the Southern Ocean:
909   Improvement of an extended OMP (eOMP) analysis, PROG OCEANOGR, 103, pp: 92-105,
910   https://doi.org/10.1016/j.pocean.2012.06.002, 2012.

911   Polyakov, I. V., Alkire, M. B., Bluhm, B. A., Brown,K. A., Carmack, E. C.,
912   Chierici, M., Danielson, S. L.,Ellingsen, I., Ershova, E. A., Gårdfeldt, K., Ingvaldsen, R.B.,
913   Pnyushkov, A. V., Slagstad, D., and Wassmann, P.: Bo-realization of the Arctic Ocean in
914   Response to AnomalousAdvection From Sub-Arctic Seas, Front. Mar. Sci., 7,
915   491,https://doi.org/10.3389/fmars.2020.00491, 2020.

916   Polyakov, I. V., Pnyushkov, A. V., Alkire, M. B., Ashik, I. M., Bau-mann, T. M., Carmack, E. C.,
917   Goszczko, I., Guthrie, J., Ivanov, V.V., Kanzow, T., Krishfield, R., Kwok, R., Sundfjord, A.,
918   Morison,J., Rember, R., and Yulin, A.: Greater role for Atlantic inflows onsea-ice loss in the Eurasian
919   Basin of the Arctic Ocean, Science,356, 285–291, https://doi.org/10.1126/science.aai8204, 2017.

920   Prinsenberg, S. J. and Bennetr, E. B.: Transport between Peel Sound and Barrow Strait in the Canadian
921   Arctic, Continental Shelf Research, 427–444 pp., 1989.

922   Radajewski S, Webster G, Reay DS, Morris SA, Ineson P, Nedwell DB, Prosser JI, Murrell JC.
923   Identification of active methylotroph populations in an acidic forest soil by stable-isotope probing.
924   Microbiology. 148(Pt 8):2331-2342. doi: 10.1099/00221287-148-8-2331. PMID: 12177327, 2002.

925   Redmond MC, Valentine DL. Natural gas and temperature structured a microbial community response
926   to the Deepwater Horizon oil spill. Proc Natl Acad Sci U S A. 2012 Dec 11;109(50):20292-7. doi:
927   10.1073/pnas.1108756108. Epub 2011 Oct 3. PMID: 21969552; PMCID: PMC3528494, 2011.

928   Repeta, D. J., Ferrón, S., Sosa, O. A., Johnson, C. G., Repeta, L. D., Acker, M., Delong, E. F., and Karl,
929   D. M.: Marine methane paradox explained by bacterial degradation of dissolved organic matter, Nat
930   Geosci, 9, 884–887, https://doi.org/10.1038/ngeo2837, 2016.

Biogeosciences

Discussions

Open Access

EGU

931   Rojo, F.: Degradation of alkanes by bacteria: Minireview, https://doi.org/10.1111/j.1462-
932   2920.2009.01948.x, 2009.

933   Saunois, M., R. Stavert, A., Poulter, B., Bousquet, P., G. Canadell, J., B. Jackson, R., A. Raymond, P.,
934   J. Dlugokencky, E., Houweling, S., K. Patra, P., Ciais, P., K. Arora, V., Bastviken, D., Bergamaschi,
935   P., R. Blake, D., Brailsford, G., Bruhwiler, L., M. Carlson, K., Carrol, M., Castaldi, S., Chandra, N.,
936   Crevoisier, C., M. Crill, P., Covey, K., L. Curry, C., Etiope, G., Frankenberg, C., Gedney, N., I.
937   Hegglin, M., Höglund-Isaksson, L., Hugelius, G., Ishizawa, M., Ito, A., Janssens-Maenhout, G., M.
938   Jensen, K., Joos, F., Kleinen, T., B. Krummel, P., L. Langenfelds, R., G. Laruelle, G., Liu, L., MacHida,
939   T., Maksyutov, S., C. McDonald, K., McNorton, J., A. Miller, P., R. Melton, J., Morino, I., Müller, J.,
940   Murguia-Flores, F., Naik, V., Niwa, Y., Noce, S., O'Doherty, S., J. Parker, R., Peng, C., Peng, S., P.
941   Peters, G., Prigent, C., Prinn, R., Ramonet, M., Regnier, P., J. Riley, W., A. Rosentreter, J., Segers, A.,
942   J. Simpson, I., Shi, H., J. Smith, S., Paul Steele, L., F. Thornton, B., Tian, H., Tohjima, Y., N. Tubiello,
943   F., Tsuruta, A., Viovy, N., Voulgarakis, A., S. Weber, T., van Weele, M., R. Van Der Werf, G., F.
944   Weiss, R., Worthy, D., Wunch, D., Yin, Y., Yoshida, Y., Zhang, W., Zhang, Z., Zhao, Y., Zheng, B.,
945   Zhu, Q., Zhu, Q., and Zhuang, Q.: The global methane budget 2000-2017, Earth Syst Sci Data, 12,
946   1561–1623, https://doi.org/10.5194/essd-12-1561-2020, 2020.

947   Shakhova, N., Semiletov, I., Leifer, I. et al. Ebullition and storm-induced methane release from the East
948   Siberian Arctic Shelf. Nature Geosci 7, 64–70. https://doi.org/10.1038/ngeo2007, 2014.

949   Silyakova, A., and others. Physical controls of dynamics of methane venting from a shallow seep area
950   west of Svalbard. Cont. Shelf Res. 194: 104030, 2020.

951   Singh, B., Bardgett, R., Smith, P. et al. Microorganisms and climate change: terrestrial feedbacks and
952   mitigation options. Nat Rev Microbiol 8, 779–790. https://doi.org/10.1038/nrmicro2439, 2010.

953   Song, J., Choi, A., Im, M., Joung, Y., Yoshizawa, S., Cho, J. C., and Kogure, K.: Aurantivirga profunda
954   gen. nov sp. nov isolated from deep-seawater, a novel member of the family flavobacteriaceae, Int J
955   Syst Evol Microbiol, 65, 4850–4856, https://doi.org/10.1099/ijsem.0.000662, 2015.

956   Sosa, O. A., Burrell, T. J., Wilson, S. T., Foreman, R. K., Karl, D. M., and Repeta, D. J.: Phosphonate
957   cycling supports methane and ethylene supersaturation in the phosphate-depleted western North
958   Atlantic Ocean, Limnol Oceanogr, 65, 2443–2459, https://doi.org/10.1002/lno.11463, 2020.

959   Spreen, G., Kaleschke, L., and Heygster, G. Sea ice remote sensing using AMSR-E 89-GHz channels,
960   J. Geophys. Res., 113, C02S03, doi:10.1029/2005JC003384, 2008.

961   Steinle, L., Graves, C., Treude,T., Ferre, B., Biastoch, A., Bussmann, I., Berndt, C., Krastel, S., James,
962   R. H., Behrens, E., Böning, C.W., Greinert, J., Sapart, C-J., Scheinert, M., Sommer, S., Lehmann,
963   Moritz F., Niemann, H. Methane concentration, oxidation rates and abundance of bacteria during Maria
964   S. Merian cruise MSM21/4 at Svalbard seeps in summer 2012. PANGAEA,
965   https://doi.org/10.1594/PANGAEA.844010, In supplement to: Steinle, L et al. (2015): Water column
966   methanotrophy controlled by a rapid oceanographic switch. Nature Geoscience, 8(5), 378–382,
967   https://doi.org/10.1038/ngeo2420, 2015.

968   Sterner, Robert W. and James J. Elser. Ecological Stoichiometry: The Biology of Elements from
969   Molecules to the Biosphere. 2002

970   Stigebrandt, A. 15200485 - Journal of Physical Oceanography] The North Pacific_ A Global-Scale
971   Estuary, 1984.

972   Sultan, N., Plaza-Faverola, A., Vadakkepuliyambatta, S., Buenz, S., and Knies, J.: Impact of tides and
973   sea-level on deep-sea Arctic methane emissions, Nat Commun, 11, https://doi.org/10.1038/s41467-
974   020-18899-3, 2020.

975   Tomczak, M. A multi-parameter extension of temperature/salinity diagram techniques for the analysis
976   of non-isopycnal mixing. *Progress in Oceanography, 10*, 147-171, 1981.

977   Tomczak, M., and Large, D. G. B. (1989), Optimum multiparameter analysis of mixing in the
978   thermocline of the eastern Indian Ocean, J. Geophys. Res., 94(C11), 16141– 16149,
979   doi:10.1029/JC094iC11p16141.Torres-Valdés, S., Tsubouchi, T., Bacon, S., Naveira-Garabato, A. C.,
980   Sanders, R., McLaughlin, F. A., Petrie, B., Kattner, G., Azetsu-Scott, K., and Whitledge, T. E.: Export
981   of nutrients from the Arctic Ocean, J Geophys Res Oceans, 118, 1625–1644,
982   https://doi.org/10.1002/jgrc.20063, 2013.

983   Torres-Valdés, S., Tsubouchi, T., Bacon, S., Naveira-Garabato, A. C., Sanders, R., McLaughlin, F. A.,
984   Petrie, B., Kattner, G., Azetsu-Scott, K., and Whitledge, T. E. Export of nutrients from the Arctic
985   Ocean, J. Geophys. Res. Oceans, 118, 1625– 1644, doi:10.1002/jgrc.20063, 2013.

986   Uhlig, C. and Loose, B. Using stable isotopes and gas concentrations for independent constraints on
987   microbial methane oxidation at Arctic Ocean temperatures. Limnol. Oceanogr. Methods, 15: 737-751.
988   https://doi.org/10.1002/lom3.10199, 2017.

989   Uhlig, C., Kirkpatrick, J. B., D'Hondt, S., and Loose, B.: Methane-oxidizing seawater microbial
990   communities from an Arctic shelf, Biogeosciences, 15, 3311–3329, https://doi.org/10.5194/bg-15-
991   3311-2018, 2018.

992   Valentine D.W., Holland E.A. & Schimel D.S. Ecosystem and physiological controls over methane
993   production in northern wetlands. Journal of Geophysical Research: Atmospheres, 99, 1563– 1571,
994   1994.

995   Verdugo, J., Damm, E., and Nikolopoulos, A.: Methane cycling within sea ice: results from drifting ice
996   during late spring, north of Svalbard, The Cryosphere, 15, 2701–2717, https://doi.org/10.5194/tc-15-
997   2701-2021, 2021.

998   Wang, Y., Yu, M., Austin, B., and Zhang, X. H.: Oleispira lenta sp. nov., a novel marine bacterium
999   isolated from Yellow sea coastal seawater in Qingdao, China, Antonie van Leeuwenhoek, International
1000 Journal of General and Molecular Microbiology, 101, 787–794, https://doi.org/10.1007/s10482-011-
1001 9693-8, 2012.

1002 Whitmore, L. M., Pasqualini, A., Newton, R., and Shiller, A. M.: Gallium: A New Tracer of Pacific
1003 Water in the Arctic Ocean, J Geophys Res Oceans, 125, https://doi.org/10.1029/2019JC015842, 2020.

1004 Yamamoto, Sachio et al. "Solubility of methane in distilled water and seawater." Journal of Chemical
1005 & Engineering Data 21, 78-80, 1976.